Deep Seek to the Excited States: A Thermally-Activated Jahn–Teller Effect Achieves Superior Sensitivity for Thermometry at Cryogenic Temperature

Weihao Wang, Fang Zeng, Guixin Liu, Shihan Xia, Yuhui Zheng, Markus Suta and Qianming Wang

Article - Version of Record

Suggested Citation:
Wang, W., Zeng, F., Liu, G., Xia, S., Zheng, Y., Suta, M., & Wang, Q. (2025). Deep Seek to the Excited States: A Thermally-Activated Jahn–Teller Effect Achieves Superior Sensitivity for Thermometry at Cryogenic Temperature. Advanced Optical Materials, 13(32), Article e02180.
https://doi.org/10.1002/adom.202502180

ADVANCED OPTICAL MATERIALS
www.advopticalmat.de

Deep Seek to the Excited States: A Thermally-Activated Jahn–Teller Effect Achieves Superior Sensitivity for Thermometry at Cryogenic Temperature

Weihao Wang, Fang Zeng, Guixin Liu, Shihan Xia, Yuhui Zheng, Markus Suta, and Qianming Wang**

Boltzmann equilibrium is not always achieved at the lower temperature limit for a typical ratiometric thermometer with thermally coupled excited states. The universal approach to broaden the dynamic temperature range of all Boltzmann-type thermometers still remains a challenge. Herein, a bismuth-based halide single crystal (DMA_4BiCl_7: Sb^{3+}, DMA is referred to as dimethylammonium) shifts the onset temperature by ≈200 K. It also provides trustworthy experimental evidence in observing a thermally-driven process from $^3P_1$ state to A_T minima. The action of both spin-orbit coupling and the dynamic Jahn–Teller effect represented by large effective Huang-Rhys factors ($S_1 = 32.44$, $S_2 = 42.51$) is responsible for maximizing the opposite emission changes at different temperatures and overcomes the thermodynamic limitations of the traditional thermally coupled energy levels. A high relative sensitivity (S_r) value of 18.9 % K^{-1} is obtained at 77 K. It finds application potential in extending the temperature window to cover the cryogenic range from 77 K to 277 K with constantly high accuracy (temperature uncertainty $\delta T = 0.065$ K at 77 K). Moreover, a new way is developed to visualize temperature mapping via grayscale imaging tools in determining the temperature distribution of a real sample is demonstrated. **anti-thermal quenching; hybrid metal halide; temperature mapping; thermally activated; thermometer**

1. Introduction

Accurate determination of ultra-low temperatures below 100 K becomes essential in various fields, including superconducting quantum techniques, aerospace, and cryogenic biological conditions.[1–4] Conventional thermometry relying on liquid expansion or resistance-type sensors requires physical contact of the detector with the objects, and the strategy possesses several disadvantages, such as slow response speed, limited accuracy, and low spatial resolution. In contrast, the alternative approach of remote temperature sensing based on luminescence signals effectively circumvents the obstacle when it is inconvenient to make direct contact with the surface being measured.[5–8]

Despite its simplicity and self-indicating feature, a ratiometric luminescent detection concept based on the radiative emission from multiple excited states is forced to vary substantially in an observable short range so as to maintain the sensitivity of the thermometer. How to keep the balance between precise determination and a wide dynamic sensing range is still challenging. In addition, Boltzmann-based thermometers suffer from both a thermodynamic and kinetic weakness. The nonradiative processes relying on the thermal occupation of phonon modes slow down at lower temperatures, which then cannot compete with radiative or any additional decay channel of one of the two excited levels anymore.[9–12] In that limit, the excited levels decouple, and thermometry is kinetically inhibited.

Trivalent lanthanoid ions with their sufficiently narrow $4f^n \leftrightarrow 4f^n$ transitions are particularly well suited for this type of thermometry.[13–16] A significant problem of the trivalent lanthanoid ions is, however, their generally low absorption cross-section that typically requires laser excitation for high luminescence brightness in real-case applications of luminescent thermometry. A recently emerged alternative in this respect are ns^2 ions such as Pb^{2+} or Sb^{3+} in halide systems because of their easy operation, solution processability, and remarkable optoelectronic properties.[17–19] The slower and delicate control over its nucleation and growth processes in such a simple model will be promising to afford a metal halide single crystal with a suitable

---

W. Wang, F. Zeng, G. Liu, S. Xia, Y. Zheng, Q. Wang
School of Chemistry, Guangzhou Key Laboratory of Analytical Chemistry for Biomedicine
South China Normal University
Guangzhou 510006, P. R. China
E-mail: qmwang@scnu.edu.cn

M. Suta
Inorganic Photoactive Materials
Institute of Inorganic Chemistry
Faculty of Mathematics and Natural Sciences
Heinrich Heine University Düsseldorf
Universitätsstraße 1, 40225 Düsseldorf, Germany
E-mail: markus.suta@hhu.de

The ORCID identification number(s) for the author(s) of this article can be found under https://doi.org/10.1002/adom.202502180

DOI: 10.1002/adom.202502180

size for structural analysis. Although the crystallographic model could ultimately give a comprehensive map of the geometry, conformation, and intermolecular interactions, the in-depth study of the effect of temperature on metal halide-related emission behavior is far from detailed.[20]

Generally, the incorporation of ns^2 ions leads to broad-band absorption in the UV range based on an $ns^1np^1 \leftarrow ns^2$ transition. However, there is usually a strong degree of excited-state relaxation that leads to large Stokes shifts, high emission band widths, and consequently, low thermal quenching temperatures.[21–23] In this way, the temperature sensing strategy has been established on the thermal quenching of luminescence.[5,24] Consequently, an experimental model of how the temperature range for thermal equilibrium can be extended to reach even the cryogenic window for precisely determining elevated temperature may be beneficial for a more targeted design.[25,26] A recent work proposed to utilize the opposite luminescence response trends at low temperatures for sensing purposes, which could reach the value of S_r = 4.23 % K^{-1} at 160 K.[27] A similar approach was provided by utilizing the two fluorescent signals derived from Sb^{3+}-activated metal halides to achieve a S_r = 4.54% K^{-1} at 80 K.[28]

Generally, the high flexibility within the structure of halides and the presence of isolated $[SbCl_6]^{3-}$ octahedra enable large Huang-Rhys-Pekar parameters S and, consequently, larger Stokes shifts and emission full widths at half maximum, which generally imply low thermal quenching temperatures.[26–29] The most challenging work lies in the realization of a limitation of thermal quenching for such emitters, which are additionally prone to dynamic Jahn–Teller coupling in the excited state. It has been well documented that the metal with ns^2 electron structure could lead to bright emission in halide, and researchers have tried to correlate the ns^2 emission with so-called negative thermal quenching.[30–32] But all the current study falls short of providing clear evidence to support the existence of thermally activated distorted-type luminescence.

Herein, the temperature-dependent optical properties of the 0D organic-inorganic, Sb^{3+}-activated hybrid halide $DMA_4BiCl_7:Sb^{3+}$ (DMA = dimethylammonium, $(H_3C)_2NH_2{}^+$) were investigated. Upon irradiation at 304 nm, this compound shows classic thermal quenching of the emission, whereas a ≈ 70-fold increase of emission intensity has been found in the temperature range of 77–277 K when Sb^{3+} is excited to the excited $^3P_1$ spin-orbit level of the $5s^15p^1$ configuration (λ_{ex} = 377 nm). The traditional theoretical description for the $5s^2$ two-electron Seitz model verifies the inevitable crossing of the ground and excited state parabolas to explain the nonradiative relaxation pathway (Figure S1a, Supporting Information, referring to the thermal quenching excited at 304 nm).[31] Nevertheless, the ultra-fast growth of emission signal from 77 K to 277 K (λ_{ex} = 377 nm) clearly suggests a double-well structure of the $^3P_1$ excited state potential energy surface, and the distorted energy states should impose an energy barrier required to overcome for an ultimate radiative process (Figure S1b, Supporting Information). It combines high brightness over a wide temperature range with a constantly high relative sensitivity S_r. Such a strategy based on opposite temperature response tendency leads to an overall high precision for the temperature read-out, beneficial to extend this concept of remote temperature sensing to the low-temperature limit.

2. Results and Discussion

2.1. Crystal Structure and Thermal Stability

The 0D bismuth-based halide DMA_4BiCl_7 ($DMA^+ = NH_2(Me)_2{}^+$) was synthesized by a solvent evaporation method. It is known from the isotypically crystallizing compound DMA_4BiBr_7 that it can form enantiomorphic crystals via chiral molecular induction based on their orthorhombic $P2_12_12$ (no. 18) space group.[33] In this work, an exchange of bromide by chloride ions was employed to obtain the desired host compound (DMA_4BiCl_7). Intrinsically, it would be inconvenient to obtain large halide single crystals (average level up to 4–6 mm), and the fine control over the nucleation density and fast growth of crystallites could be elusive. To grow single crystals with more stable opto-electronic performance and fewer defects or grain boundaries, well-defined, reproducible, and easily adjustable procedures are highly desirable. In this work, the controllable growth was realized by the stepwise cooling precipitation, achieving a maximum size of either 1.5 cm × 1.0 cm in lateral dimension (Figure S2, Supporting Information). Single-crystalline DMA_4BiCl_7 indeed crystallized in a $P2_12_12$ (no. 18) space group without any chiral components. Figure S2a (Supporting Information) shows the schematic diagram for the synthesis of the single crystals. Dimethylamine hydrochloride was cooled in an ice bath before being added to a Bi^{3+}-containing solution upon temperature rise. The whole mixture was diluted and finally cooled to obtain single crystals. Single-crystal X-ray diffraction (SCXRD) on the thus obtained crystals proved the space group with cell parameters a = 10.2773 Å, b = 13.3871 Å, c = 8.5496 Å. More details are displayed in Table S1 (Supporting Information). The structure is related to a distorted variant of the elpasolite-type structure (formally DMA_3BiCl_6) with additionally intercalated (DMA)Cl layers, in which the Cl^- ions are sixfold disordered. Thus, the structure may be described as $DMA_3((DMA)Cl)[BiCl_6]$.[34,35] The Bi^{3+} ions are nearly perfectly octahedrally coordinated by six Cl^- ions, while the DMA^+ cations additionally strengthen the structure by a hydrogen bonding network (see Figure S2b, Supporting Information). The detailed SCXRD measurement data are displayed in Table S1 (Supporting Information). The $[BiCl_6]^{3-}$ octahedra are isolated within the structure, and the $6s^2$ lone pair is not stereochemically active. The single crystal is colorless and transparent under daylight irradiation. Upon activation with 50 mol% Sb^{3+}, $DMA_4Bi_{0.5}Sb_{0.5}Cl_7$ produces a bright orange–red luminescence when exposed to UV light at 365 nm (Figure S2c, Supporting Information).

The thermal stability of $DMA_4BiCl_7:Sb^{3+}$ was measured by in situ temperature-dependent XRD and thermal gravimetric analyses (TGA). The results (**Figure 1a,b**) reveal that the crystal structure does not change in the temperature range between 103 and 303 K, and the stability of the orthorhombic phase could be enough in the regarded range. It is known that these compounds tend to lose (DMA)Cl at high temperatures, thus forming DMA_3BiCl_6.[35] The Bragg reflections shift to lower angles with increasing temperatures, indicating an expansion of the cell volume reversibly in the range between 103 K and 303 K. The TGA results confirm that the material is stable below 473 K and a weight loss between 323 K and 373 K is ascribed to solvent volatilization. As depicted in Figure 1c, the 3d electrons of Sb were measured by X-ray photoelectron spectroscopy (XPS),

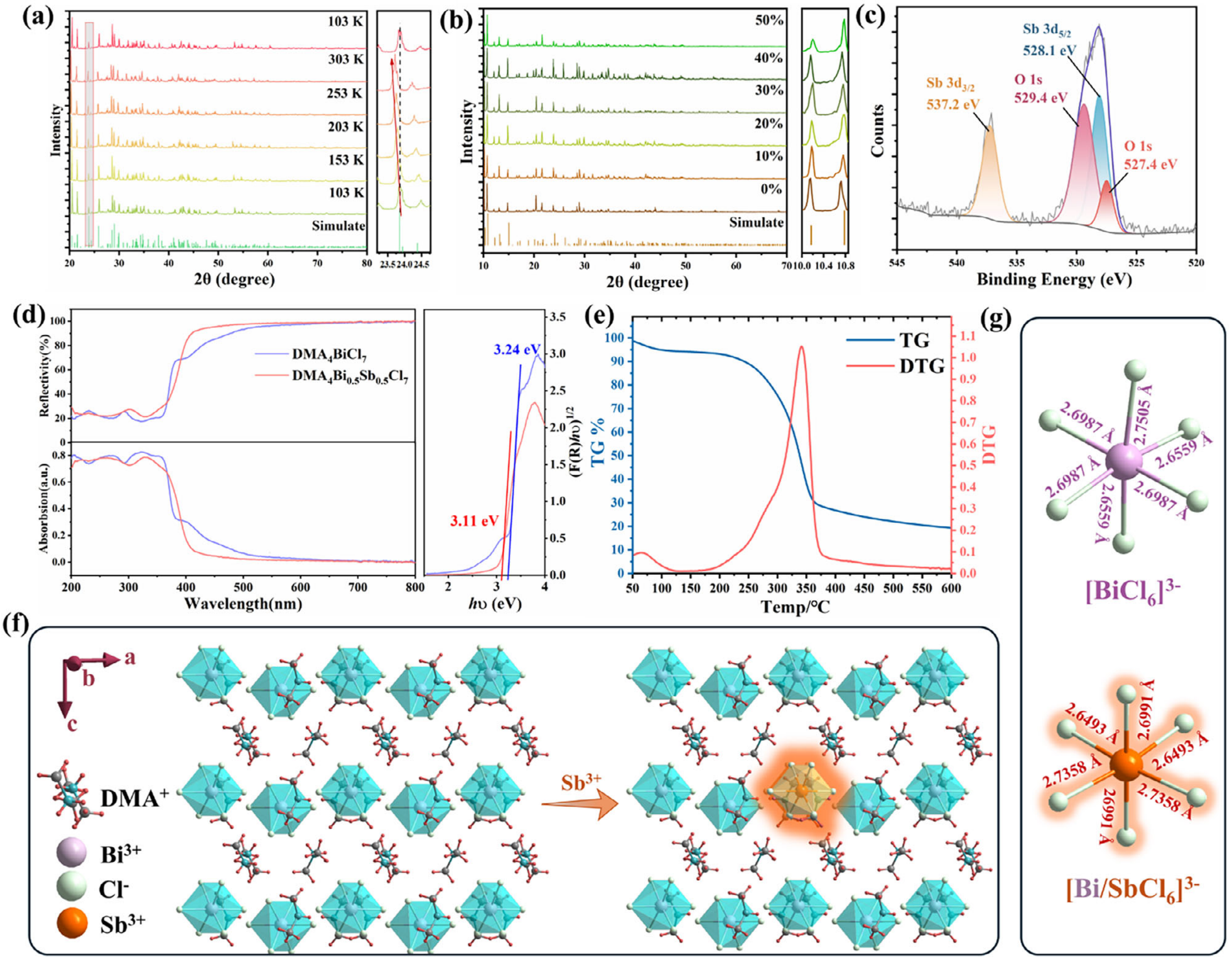

Figure 1. a) Variable temperature PXRD pattern of $DMA_4Bi_{0.5}Sb_{0.5}Cl_7$. b) PXRD patterns of DMA_4BiCl_7: xSb^{3+} (x = 0–50%). c) XPS spectrum of Sb 3d in $DMA_4Bi_{0.5}Sb_{0.5}Cl_7$. d) UV/Vis optical absorption spectra and reflectance spectra of undoped and Sb^{3+}-doped DMA_4BiCl_7. e) Thermogravimetric analyses of the single crystal. f) Local crystal structure of DMA_4BiCl_7 and Sb^{3+}-doped DMA_4BiCl_7. g) Coordination environments of $[MCl_6]^{3-}$ unit labeled with bond lengths.

and the overlapping O1s peaks were possibly attributed to oxygen atoms from residual water attached onto the surface. The full spectrum of the XPS analysis represents the presence of elements including C, N, Cl, and Bi (Figure S3, Supporting Information). As shown in Figure S4 (Supporting Information), scanning electron microscopy (SEM) can also prove the incorporation of Sb^{3+}, and elemental mapping shows the uniform distribution of various elements in the crystal. The bandgap of the samples before and after Sb^{3+} activation was analyzed by ultraviolet-visible (UV–Vis) spectroscopy (shown in Figure 1d), and the bandgap changed from 3.24 to 3.11 eV due to the incorporation of Sb^{3+}. The appearance of the Tauc plots indicates an indirect bandgap. The powder X-ray diffraction (PXRD) results showed that a subtle change was observed upon incorporation of different Sb contents, and the very slight shift of the Bragg reflections was found due to the soft lattice structure network of the 0D metal halide (Figure 1b). In general, the ionic radius of Sb^{3+} (r = 0.76 Å, CN = 6) is much smaller than that of Bi^{3+} (r = 1.03 Å, CN = 6), the substitution of Sb^{3+} for the lattice position of Bi^{3+} should expectedly result in lattice shrinkage. However, the average bond length of metal and chloride revealed that changes were only negligible (Figure 1f,g), which may also be related to a compensating effect of the larger space that the $5s^2$ lone pair of Sb^{3+} takes compared to the more shrunk $6s^2$ inert lone pair of Bi^{3+}.[36] To further verify the exact crystal structure information, Rietveld structural refinements on XRD patterns were employed by using the GSAS program (Figure S5, Supporting Information) with very good quality parameters. The lattice parameters and the unit cell volumes were given, and a phase-pure nature was indicated in the presence of Sb^{3+}.

2.2. Luminescence Properties of Sb^{3+}-Doped DMA_4BiCl_7

Pure DMA_4BiCl_7 does not exhibit any visible photoluminescence under UV excitation at room temperature, as shown in Figure S6f (Supporting Information), the covering range of the absorption curve for the sample containing Sb^{3+} is slightly wider than the

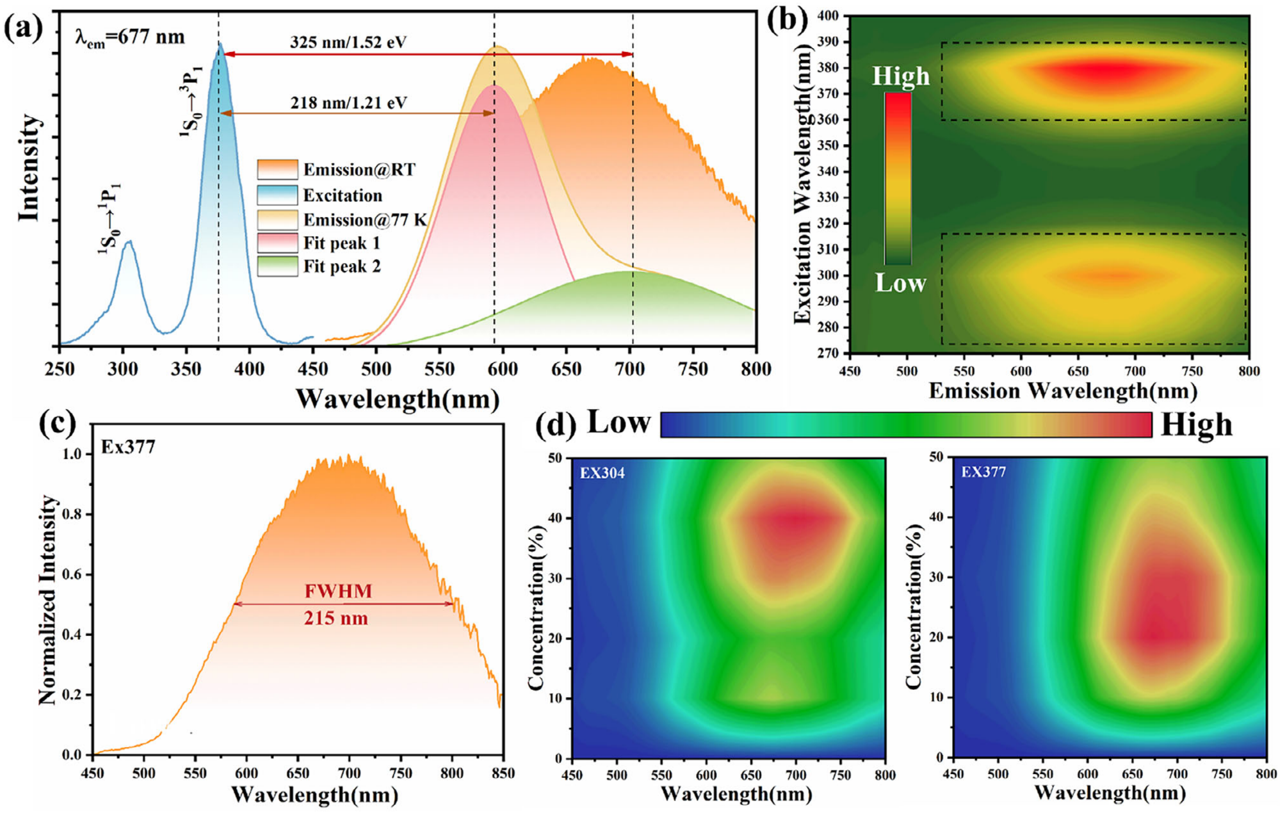

Figure 2. a) The excitation and emission spectra of DMA_4BiCl_7: Sb^{3+} at RT and emission spectrum at 77 K. b) Emission spectrum (λ_{ex} = 270–400 nm) mapping of DMA_4BiCl_7: Sb^{3+} at RT. c) The FWHM of emission at RT (λ_{ex} = 377 nm). d) Emission spectra of DMA_4BiCl_7: xSb^{3+} (x = 0–50%, and λ_{ex} = 377 or 304 nm).

undoped sample, and the band is gradually red-shifted (Figure S6e, Supporting Information). It shows a bright orange-yellow luminescence under UV light excitation after incorporation of Sb^{3+} activators, and the absorption, PLE, and PL spectra indicate that the photoluminescence is driven by Sb^{3+}-doping. The presence of $[SbCl_6]^{3-}$ centers leads to broad-band luminescence based on a $5s^15p^1 \rightarrow 5s^2$ transition. The primary luminescence properties of DMA_4BiCl_7: Sb^{3+} are summarized in **Figure** 2a. The appearance of the emission spectra shows a strong dependence on temperature. At room temperature, the Sb^{3+}-activated compound shows red emission peaking at 677 nm, while it becomes blue-shifted into the orange–yellow range at 595 nm at 77 K. The variation in the emission color is also reflected in the change of its CIE chromaticity coordinates. The coordinates evolve from (0.5291, 0.4611) at 77 K to (0.5604, 0.4138) at room temperature. Their positions and shifting routes are plotted and provided in Figure S7 (Supporting Information). At low temperature (λ_{ex} = 304 nm), the broad emission curve is composed of two independent signals that can be easily separated by Gaussian peak fitting, with the peak maximum at 595 and 703 nm, respectively. These can be considered A_T- and A_X-type emission bands from Sb^{3+} that are usually observed if Jahn–Teller and spin-orbit coupling in the excited state have similar contributions and give rise to a double-well potential energy surface of the excited $^3P_1$ level in the configurational coordinate space. In previous literature, there were A, B, C, and D bands observed in the absorption profiles of alkali halides containing ns^2 configuration dopants, and the A band was the lowest one in energy. The two separated emission peaks following A-band excitation were referred as A_T (high energy) and A_X (lower energy). The two signals have been determined by strong coupling or interplay between Jahn–Teller effect and spin-orbit interaction.[36–38] Upon higher-energy excitation at 304 nm, the blue-shifted A_T-type emission is observed. While at higher temperatures, the A_X-type emission evolves related to thermal activation over a barrier between the two potential well minima on the $^3P_1$ energy surface. Excitation at lower energies (λ_{ex} = 377 nm), however, only leads to the dominant observation of the red-shifted emission at ≈703 nm.

When monitoring the luminescence at 677 nm, its excitation spectrum includes two prominent bands, which are assigned to the electron transition from $5s^15p^1 \leftarrow 5s^2$ of Sb^{3+}, and the corresponding spectral transitions are termed as $^1P_1 \leftarrow {}^1S_0$ (C band) and $^3P_1 \leftarrow {}^1S_0$ (A band).[36] The full schematic diagram is given in Figure S8 (Supporting Information). The luminescence decay curves excited by 304 or 377 nm irradiation are represented in Figure S9a (Supporting Information) with average lifetimes (τ_{ave}) of 24.15 and 29.76 µs. The photoluminescence quantum yield (PLQY) has been calculated by integrating sphere spectral data, and the value (34.7%) is given in Figure S9b (Supporting Information). The large Stokes shifts of 1.52 eV (for C band) and 1.21 eV (for A band), as well as the recorded broad band, indicate the extensive degree of excited-state relaxation, which is common to ns^2 ions. To gain more insights into the photophysical process, the emission profiles at different excitation wavelengths were measured in Figure 2b, and the spectral mapping results had no band shifts collected with an excitation wavelength varying from 270 to 390 nm. It could be verified that only one emitting center is present within the crystalline structure, and all the signal is generated by the luminescence of the incorporated Sb^{3+} ions. The influence of the organic moiety DMA^+ and the inorganic host $[BiCl_6]^{3-}$ in the crystal on the emission appears to be negligible (Figure 2c). The Inductively coupled plasma optical emission spectrometer (ICP-OES) results indicated that the actual doping ratio is similar to the raw input ratio (Table S2, Supporting Information). Upon increase of the Sb^{3+} activator concentration from 0% to 50 % (Figure 2d), the appearance of the emission spectra did not change, indicating a negligible effect of structural distortion upon incorporation of the Sb^{3+} ions into the host structure.

2.3. Theoretical Calculations

The differences in the electronic structure of DMA_4BiCl_7 and DMA_4BiCl_7: Sb^{3+} were addressed by density functional theory (DFT) calculations. The electronic band structures of DMA_4BiCl_7 and DMA_4BiCl_7: Sb^{3+} are depicted in Figure S10a,b (Supporting Information). The flat energy bands indicate that the electron distribution is highly localized, which is consistent with the sharp peaks in the density of state (DOS) diagram (shown in Figure S10c,d, Supporting Information). Based on the above calculation, the electrons would be highly confined within the independent structural units to form localized excitons and such a fact is in good agreement with the 0D structure of the single crystal, as analyzed by the structural analysis, where the isolated $[MCl_6]^{3-}$ (M = Bi/Sb) octahedra are anchored in a hydrogen bonding network of DMA^+. In addition, the CBM and VBM contain strong contributions from the s or p orbitals of the s^2 ion Bi or Sb, respectively, suggesting that the electronic transition is rather localized (Figure S10e,f, Supporting Information). This is in good agreement with the previous interpretation of the luminescence spectra.

Both DMA_4BiCl_7 and DMA_4BiCl_7: Sb^{3+} exhibit indirect bandgaps in line with the observation from the Tauc plots (see Figure 2d) with estimated values of 4.12 and 3.61 eV. Apparently, the bandgap is reduced upon incorporation of Sb^{3+} ions into the host structure. The valence band maximum (VBM) of DMA_4BiCl_7 mainly contains contributions from the inert 6s orbitals of Bi and the 3p orbitals of Cl, while the conduction band minimum (CBM) is dominantly formed by contributions from the Bi 6p orbitals and the Cl 3p orbitals. After activation with Sb^{3+}, the chemically less inert and thus, energetically raised 5s orbitals of Sb take part in the contribution of the VBM, and its 5p orbitals incorporate into the energy level of the CBM, resulting in a generally lowered value of the bandgap.

2.4. Thermal Response and Mechanism Analysis

In order to investigate the functionality of the DMA_4BiCl_7: Sb^{3+} as a ratiometric luminescent thermometer, temperature-dependent steady-state emission spectra were recorded upon excitation with 304 and 377 nm, respectively (**Figure 3**a). In both cases, the emission profiles become red-shifted as the temperature rises, and the Gaussian fitting peak-1 has gradually evolved to peak-2 in Figure 2a. The entire transition process has been demonstrated for each emission spectrum at different temperatures in Figure S11 (Supporting Information) and the intensity ratio of peak-2 versus peak-1 increases rapidly. Although peak-2 exhibits temperature-dependent changes, the integrated intensity for the whole fluorescent signal was severely suppressed, and the emission curve moved toward the low-energy range.

The two separate signals are assigned as the A_T- and A_X-type emission of the incorporated Sb^{3+} ions,[37–39] which is related to the $^3P_1 \rightarrow {}^1S_0$ transition. Both emission bands are only observed upon excitation at 304 nm ($^1P_1 \leftarrow {}^1S_0$). In contrast, there is almost no visible emission at 77 K upon excitation at 377 nm ($^3P_1 \leftarrow {}^1S_0$). Generally, the observation of two emission bands is ascribed to a dynamical Jahn-Teller effect in the excited $^3P_1$ state with two pronounced minima forming by coupling to a tetragonal (A_T) and trigonal (A_X) distorting mode. For Sb^{3+}, the explicit observation of two emission bands is rather rare,[40–43] and has so far only been reported for xenotime-type rare-earth orthophosphates $REPO_4$:Sb^{3+} (RE = Y, Lu, Sc)[44] or organic–inorganic hybrid halides with isolated $[SbCl_5]^{2-}$ units,[45] while in most other investigated hosts, only one broad band is observed.[46,47] The decay times (see Figure 3d) in the order of μs additionally indicate that emission dominantly arises from the $^3P_1$ level. The decay curves at different temperatures are depicted in Figure 3d. A thermally induced slight increase of the average decay time of the $^3P_1$-based emission is observed. Since the two bands overlap each other, A_T band evolves to A_x band by crossing the thermal barrier (ΔE_x) as the temperature increases (Figure 3e). A notable observation is the change in the luminescence color from yellow to red with the shifts of the CIE chromaticity coordinates and peak wavelengths of the sample at different temperatures (Table S3, Supporting Information).[48,49]

In line with this interpretation, the outcome of the temperature dependence of the luminescence depends on the chosen excitation wavelength. Upon excitation with 304 nm (C band excitation), the emission intensity shows a common thermal quenching behavior. In addition, the lower energetic A_X-type emission at 706 nm gains intensity at elevated temperatures compared to the higher energetic A_T-type emission at 595 nm. Upon irradiation at 377 nm that the emission shows a record-high increase of its integral intensity when the temperature is raised from 77 to 277 K (Figure 3b). Table S4 (Supporting Information) summarizes the anti-thermal quenching properties of the emission derived from the metal halide materials. This gigantic value is definitely the most prominent one and exhibits more than one order of magnitude increase compared with all the observed samples.

To vividly demonstrate the dual emission changes in DMA_4BiCl_7: Sb^{3+}, Videos S1 and S2 (Supporting Information) were also recorded for the evolution process. A luminescent film was made by laminating DMA_4BiCl_7: Sb^{3+} with PDMS. The film on a glass sheet was exposed to the liquid nitrogen to realize the condition of 77 K and the surface temperature would rise as liquid nitrogen evaporated. In Video S1 (Supporting Information), the film was excited with a UV lamp at 300 nm, and its luminescence vanished upon increasing temperature. But its

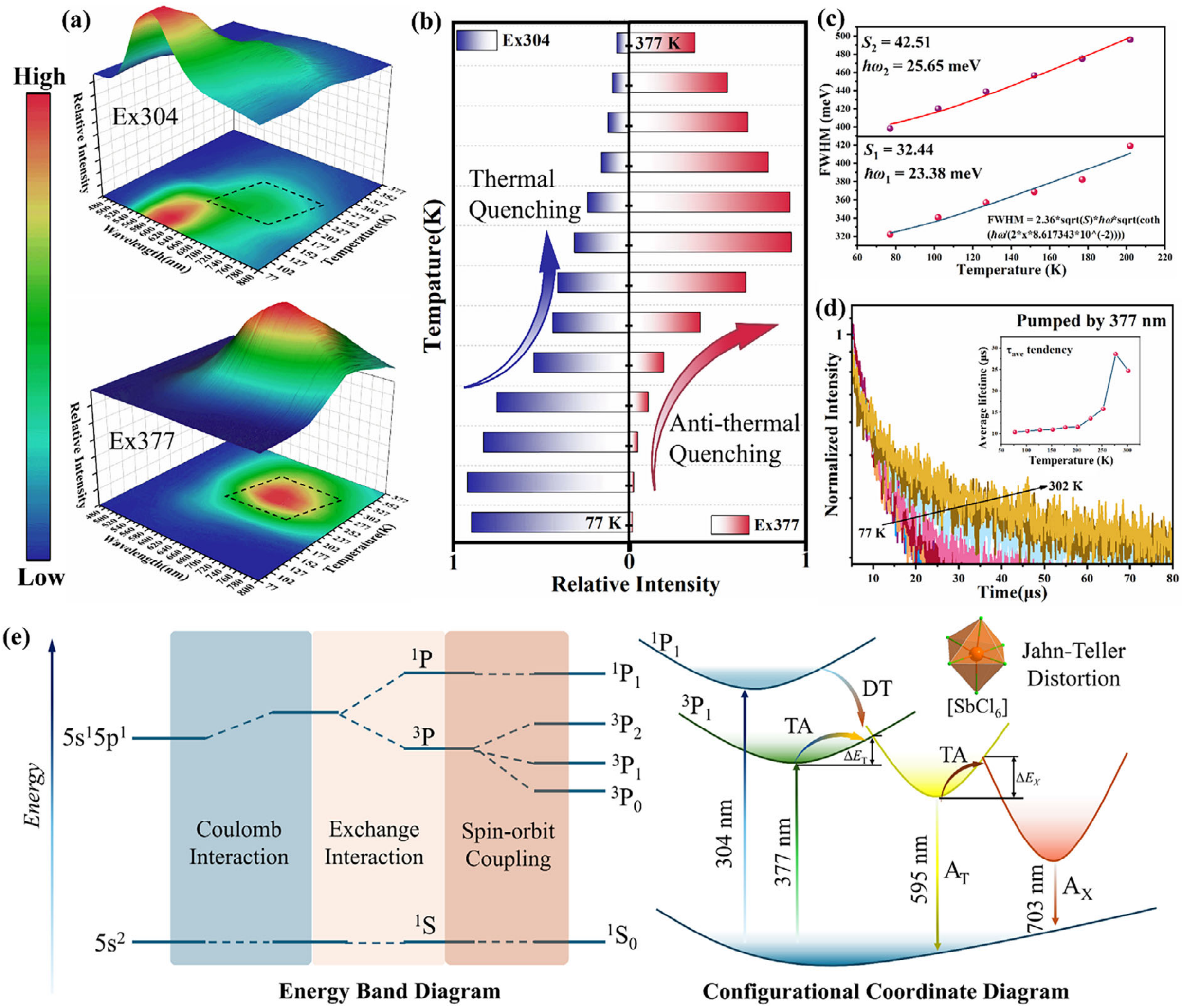

Figure 3. a) Temperature-dependent emission spectra mapping (77 K–377 K, λ_{ex} = 304 nm and 377 nm). b) The peak intensity at different temperatures (λ_{ex} = 304 nm and 377 nm). c) FWHM of DMA_4BiCl_7: Sb^{3+} as a function of temperature (λ_{ex} = 304 nm). d) Decay curve of DMA_4BiCl_7: Sb^{3+} at different temperatures. e) Luminescence mechanism schematic diagram of DMA_4BiCl_7: Sb^{3+}, here DT refers to direct transition, TA refers to thermal activation.

emitting intensity was drastically improved as the temperature was raised upon irradiation at 365 nm (Video S2, Supporting Information). Such sharp difference in emission behavior by only adjusting the excitation wavelength enlarges the intensity ratio responsive to temperature and effectively solves the problem of low thermalization rate and the lack of Boltzmann equilibrium under cryogenic conditions. In general, the emission has been additionally characterized by calculating the effective Huang–Rhys–Pekar factor (S), and different emission bands from the same emitter have diverse S values. Therefore, the S of the two states is retrieved by the FWHM of the Gaussian fitting band under different temperatures (Equation S2, Supporting Information), as shown in Figure 3c. The results reveal that S_1 = 32.44, $\hbar\omega_1$ = 23.38 meV, and S_2 = 42.51, $\hbar\omega_2$ = 25.65 meV, respectively ($\hbar\omega$ is the effective phonon energy of the mode that is coupled to electrons).

The previously mentioned observation offers a way for dual-excitation ratiometric luminescent thermometry with Sb^{3+} as a new concept. From the temperature dependence of the emission spectra and the observation of two emission bands, it becomes evident that there is a thermal activation barrier with two minima on the $^3P_1$-based potential energy surface. Such an adjusting strategy concerning the inter-excited states varies greatly from the multiple thermally-coupled energy levels within only one cation (Ln^{3+} or M^{n+}) and is particularly useful for the cryogenic temperature range, for which the other mentioned emitters often lack sufficiently fast thermalization compared to radiative decay. Upon excitation at 377 nm, we could barely observe the luminescence of the sample at 77 K without the activation of the energy barrier, but the red emission becomes intensified as the temperature rises. Under the excitation of different powers of laser, the luminescence intensity increases linearly with the power (see Figure S12, Supporting Information). This means that the anti-thermal quenching is not derived from the common mechanism of traps (traps in some materials are able to supply luminescence). Thus, according to the above analysis, we propose a new mechanism model for DMA_4BiCl_7:Sb^{3+} derived from thermally-activated Jahn–Teller distortion. Under higher energy

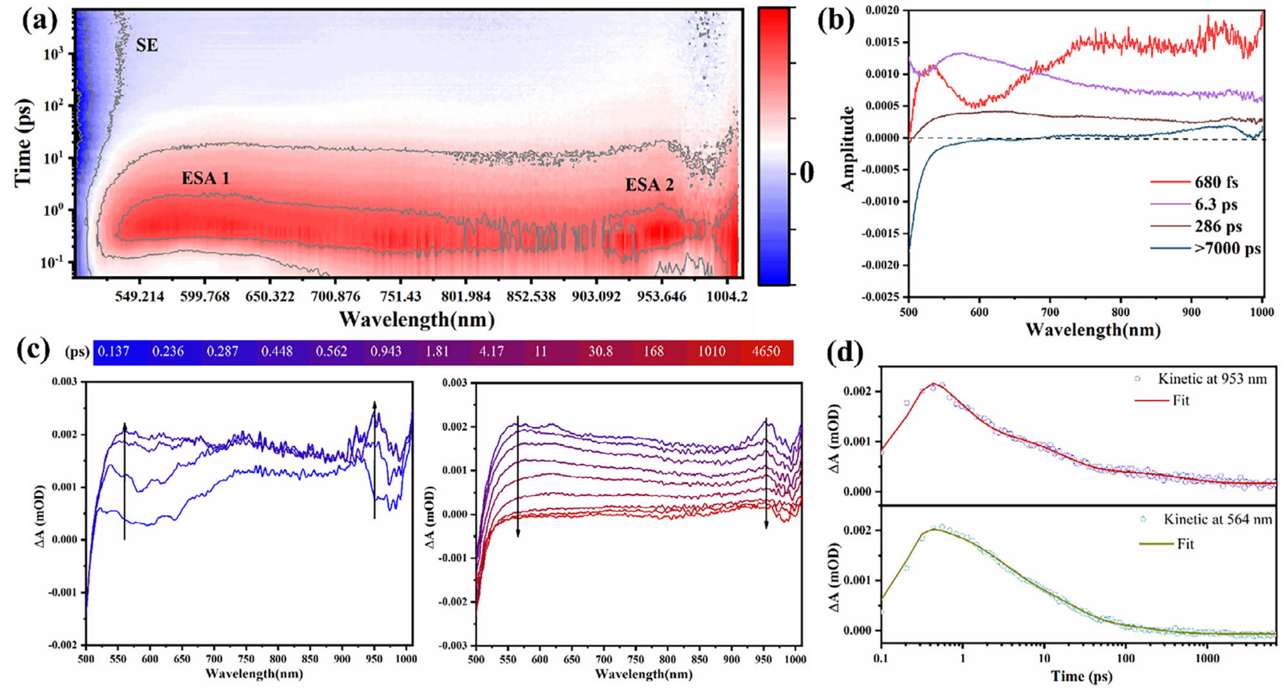

Figure 4. fs-TA measurements of DMA_4BiCl_7: Sb^{3+}. a) Contour map of TA spectrum (λ_{ex} = 343 nm, Collected range: 500–1010 nm). b) Evolution-associated spectra (EAS) components derived from SVD global fitting. c) Several time-specific TA spectra (from blue to red: 137 fs–4650 ps). d) Temporal kinetics at 564 and 953 nm.

irradiation (304 nm), the electrons are excited to $^1P_1$ and the further forbidden transition to $^3P_1$ is realized since spin-orbit coupling relaxes the selection rule. At such a higher vibration energy state, it has been perturbed by Jahn–Teller distortion to induce two minima emission states through direct transition (DT). However, in the situation excited by 377 nm, the electrons in the ground state translate to the bottom of $^3P_1$ and they require some phonon (thermal vibration) assistance to go beyond the crossing point of two parabolas through thermal activation (TA) process (Figure 3e). In this model, there are two energy barriers that control two thermally activated processes. The first one is between the $^3P_1$ and A_T emission state (ΔE_T), which is only present in the case of 377 nm excitation, resulting in thermally enhanced luminescence. Another one (ΔE_X) is between the A_T and A_X, which commonly exists within the two states, and will induce the ratio change of A_X/A_T due to the temperature rise. The synergistic effect of two thermally activated processes results in a unique feature of thermal response.

2.5. Kinetic Properties of Excited States

Excited states dynamics in semiconducting halides of the soft ns^2 ions should manifest in transient absorption spectral analysis, and a strategy of femtosecond transient absorption (fs-TA) was utilized to explore the kinetic properties of DMA_4BiCl_7:Sb^{3+} (**Figure 4**) (the detailed sample pre-treatment procedure and experimental setup guidelines are given in Supporting Information). Upon laser pulse irradiation (pump power = 25.6 mW), a broad band covering a very wide range from 500 to 1000 nm is observed. Such an excited state absorption (ESA) signal has been assigned to the contribution by the existence of A_X/A_T state (Figure 4a).[50,51]

The mixed TA spectra were processed by the singular value decomposition (SVD) method to perform global fitting, and the analysis yielded four components (τ_1 = 680 fs, τ_2 = 6.3 ps, τ_3 = 286 ps, τ_4 = 7000 ps) (Figure 4b). The extremely rich spectral dynamics were found within the first 1 ps, and clearly two individual excited states (ESA1 and ESA2) were rapidly formed in a rather short time scale, and the two positive signals were substantially improved with increasing delay time from 100 to 750 fs (Figure 4c,d). Therefore, the fact firmly supports the two emission states formed within ultrafast time (750 fs). In the time range from 6.3 to 286 ps, the ESA signal decays (Figure 4c). Finally, the decay of the ESA signal evolves to a featureless broadband at a long-lived time scale in the nanosecond range, which presents a slow decay rate and positive signal over the detecting window (7000 ps). In principle, we have demonstrated how the formation of two emission states can be employed for verifying the physical processes behind the fact of anomalous temperature response observed in DMA_4BiCl_7: Sb^{3+}. Immediately after photoexcitation, the local lattice distortion can take place and leads to the formation of Jahn–Teller distorted states in less than a picosecond.

2.6. Application

The most common way to study luminescent thermometry relies on recording variations in the emission intensity, and the

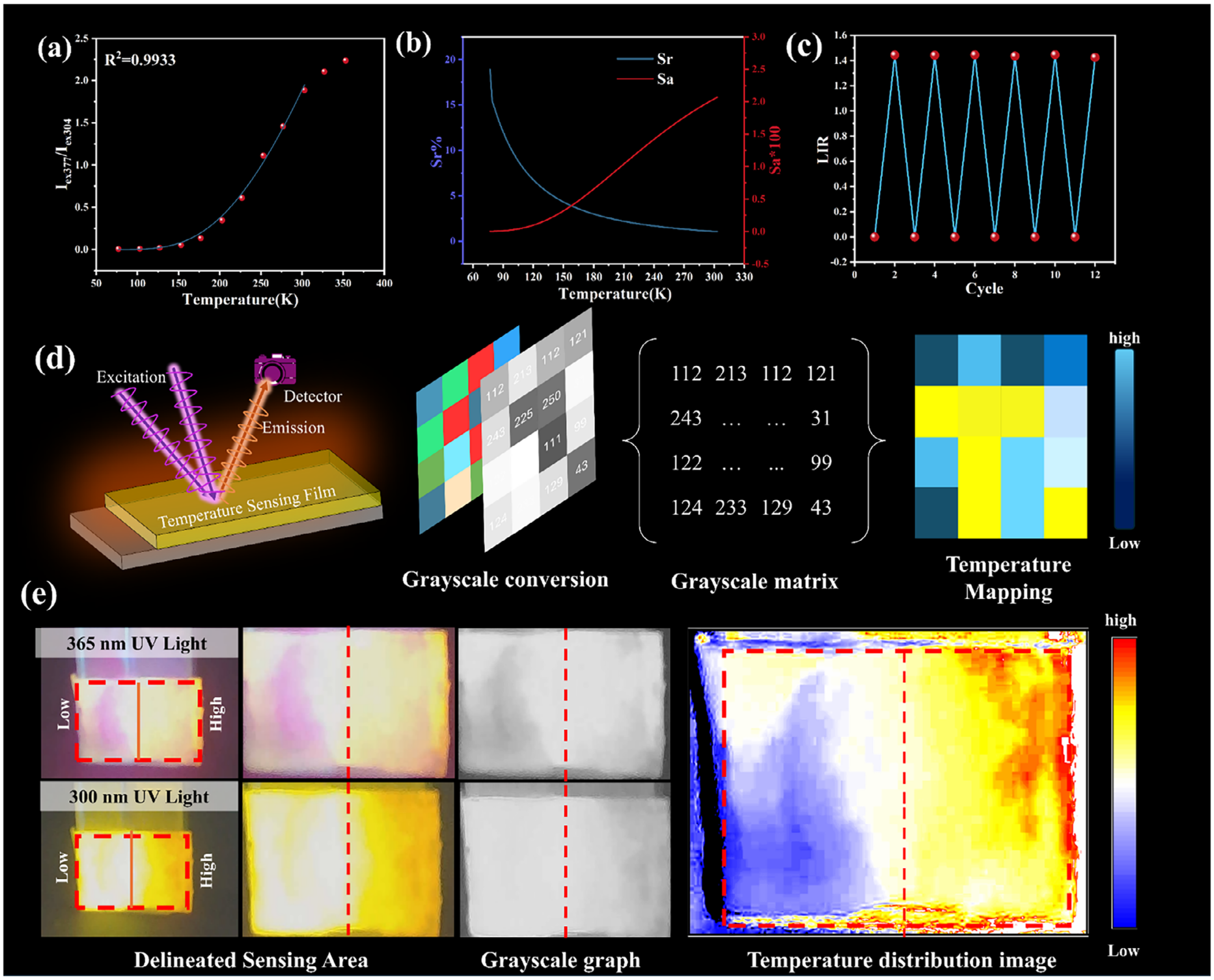

Figure 5. Application of temperature sensing. a) Fitting curve of temperature sensing. b) Sa and Sr at different temperatures. c) LIR cycle test at 77 and 277 K. d) Strategy of temperature distribution distribution. e) Temperature mapping of PDMS film onto the surface of two cuvettes with liquid hydrogen (left) and ethanol (right).

ratiometric approach offers enough stability or robustness in measurement by suppressing negative influence from a variety of factors, including excitation source intensity fluctuation, concentration of functional species, optical path change, or sample scattering.[5,23] In this work, a Sb^{3+}-activated hybrid metal halide (DMA_4BiCl_7:Sb^{3+}) has been used, and its luminescence intensity ratio (LIR) varies dramatically with temperature changes upon dual excitation at 304 or 377 nm (**Figure** 5a,c). Its LIR changes at different temperatures can fit Equation S3 (Supporting Information) well (from 77 to 302 K). According to Equation S4 (Supporting Information), the absolute sensitivity (S_a) and relative sensitivity (S_r) of the temperature measurement curve can be calculated. The S_a value has been determined to be 0.0207 K^{-1} at 302 K, and it should be emphasized that the S_r value retrieved 3 from available experimental data could reach up to 18.9% K^{-1} at 77 K.

For most conventional luminescence thermometers, the range of the temperature-sensing window is inversely related to the sensitivity metrics. In this work, excitation at 304 nm results in luminescence of the Sb^{3+} ions that is prone to common thermal quenching, while excitation at 377 nm leads to the otherwise uncommon observation of thermally enhanced luminescence in the deep red range. Figure S13 (Supporting Information) summarizes the maximum reported relative sensitivities of some common phosphors, which give rise to the good performance of this work. In addition to its high S_r at 77 K, the relative sensitivity can be maintained well above 1% K^{-1} until 302 K. To verify the stability of the thermometer, the LIR at 77 and 277 K are assessed in cycles, and the value remains essentially unchanged. Its relative uncertainty of the LIR (δLIR) is translated to the temperature uncertainty (δT) (Equation S5, Supporting Information) with the values of 0.065 K at 77 and 0.094 K at 277 K. In this regard, our dual-excitation approach easily allows precise low-temperature thermometry.

For the sake of integrating its function with artificial intelligence (AI)-programming techniques, we have developed a new approach to visualize a temperature distribution via grayscale imaging tools. Based on the temperature sensing data above, the pixel gray scale can be used instead of the luminous intensity to draw the temperature mapping (Figure 5). Initially, a temperature-sensing flexible film was made by mixing polydimethylsiloxane (PDMS) with DMA_4BiCl_7:Sb^{3+} (detailed preparation process given in the supplemental information). The robust film has outstanding mechanical properties, and its luminescence properties barely change due to the repetitive folding or twisting operation (Figure S14, Supporting Information). Video S3 (Supporting Information) also demonstrates its high water-resistant capability.

A CCD camera is used to capture the luminescence of the flexible film, and the grayscale conversion of the signal is performed based on Python + OpenCV to isolate the subject from its background (the full code has been provided in Supporting Information). In the next step, the temperature mapping can be compared to the gray matrix data at two excitation wavelengths, and the experimental analysis results are given in Figure 5e. As for the operation, the luminescence film has been put onto the surface of two cuvettes, one cuvette filled with liquid nitrogen created a temperature difference, and finally, the temperature distribution on both sides of the film has been evaluated. It gives rise to an obvious thermal quenching under the excitation at a 300 nm UV light source, whereas the irradiation at 365 nm leads to the observation of thermally induced enhancement of photoluminescence, which could be fully consistent with the results collected by a luminescence spectroscopy instrument. According to the temperature change from low to high, a clearly discernible temperature distribution image with remote detection has been realized. In addition, a real sample derived from a stainless-steel circular sheet was selected, and it was placed under a glass plate after liquid nitrogen treatment in advance (Figure S15, Supporting Information). Its low-temperature region could be visualized by the above temperature mapping method. In addition, a total of 500 grayscale recordings were made at 77 K and room temperature in a liquid nitrogen constant temperature chamber, as shown in Figure S16 (Supporting Information), demonstrating the long-term stability of the sensing film.

3. Conclusion

In summary, a 0D lead-free hybrid inorganic-organic halide (DMA_4BiCl_7: Sb^{3+}) was synthesized, and the experimental process could be controlled to grow a centimetre-scale single crystal (1.5 cm × 1.0 cm) by stepwise cooling precipitation. Its highly ordered individual octahedron units result in intensely localized charge translation with the formation of Jahn–Teller distortion, and the incorporation of Sb^{3+} ions leads to the observation of typical $5s^15p^1 \rightarrow 5s^2$ luminescence with a broad band and large Stokes shift. It dictates that the fine control over the two excited state potential (A_T and A_X minima of the $^3P_1$ level) related to a dynamic Jahn–Teller distortion has a substantial impact on the emission at cryogenic temperature. Upon excitation at 377 nm, the sample exhibits invisible emission at 77 K in the absence of thermal activation of the energy barrier. An increasing luminescence intensity has been observed as the temperature rises. Such a thermally activated process within the excited $^3P_1$ level potential results in a 68-fold improvement of the luminescence when the temperature varies from 77 to 277 K, whereas it also shows conventional thermal quenching when the electron is excited to the $^1P_1$ level (λ_{ex} = 304 nm). Based on these effects, the typical decline of relative sensitivity with increasing temperature usually encountered in luminescent thermometers has been circumvented. A well acceptable sensitivity ($S_r > 1\ \%K^{-1}$) can be realized at 302 K that significantly increases (S_r = 18.9% K^{-1}) at 77 K. This demonstrates that the strongly temperature-dependent luminescence in hybrid metal halides related to an exploitation of the excited-state dynamic Jahn–Teller effect can be used for cryogenic thermometry on purpose if carefully adjusted.

Supporting Information

Supporting Information is available from the Wiley Online Library or from the author.

Acknowledgements

Q.M. thanks grants from Guangdong Province Key Field R&D Plan Project (2024B1111100001). The authors are grateful for the assistance by the Analytical Testing Center of Guangdong University of Technology in fluorescence testing and analysis. M.S. is grateful for a scholarship by the “Young College” of the North-Rhine Westphalian Academy of Sciences, Humanities, and the Arts and a Strategic Research Fund of the Heinrich Heine University Düsseldorf. W.H. is supported by the Scientific Research Innovation Project of Graduate School of South China Normal University (2024).

Open access funding enabled and organized by Projekt DEAL.

Conflict of Interest

The authors declare no conflict of interest.

Data Availability Statement

The data that support the findings of this study are available from the corresponding author upon reasonable request.

Received: July 8, 2025
Revised: September 11, 2025
Published online: September 27, 2025

---

[1] I. S Youssefi, Y. J. Joshi, N. R. Bernier, A. Lukashchuk, P. Uhrich, L. Qiu, T. J. Kippenberg, *Nat. Electron.* **2021**, *4*, 326.
[2] C.-J. Yu, S. von Kugelgen, D. W. Laorenza, D. E. Freedman, *ACS Cent. Sci.* **2021**, *7*, 712.
[3] S. Alam, M. S. Hossain, S. R. Srinivasa, A. Aziz, *Nat. Electron.* **2023**, *6*, 185.
[4] G. Zhou, Y. Wang, Y. Mao, C. Guo, J. Zhang, M. S. Molokeev, Z. Xia, X. M. Zhang, *Adv. Funct. Mater.* **2024**, *34*, 2401860.
[5] Q. Ni, Z. Mei, C. Li, J. Li, J. Liu, W. Liu, J. Huo, Q. Wang, *Inorg. Chem.* **2021**, *60*, 19315.
[6] G. Bao, K.-L. Wong, D. Jin, P. A. Tanner, *Light: Sci. Appl.* **2018**, *7*, 96.
[7] J. Y Wen, Z. Zeng, J. Gao, Y. Zheng, *Luminescence* **2017**, *32*, 382.
[8] M. Kaczmarek, Y.-Y. Liu, M. K. Kaczmarek, H. Liu, F. Artizzu, L. D. Carlos, P. Van Der Voort, *Angew. Chem., Int. Ed.* **2020**, *59*, 1932.
[9] R. G. Geitenbeek, H. W. de Wijn, A. Meijerink, *Phys. Rev. Appl.* **2018**, *10*, 064006.
[10] M. Suta, Ž. Antić, V. Đorđević, S. Kuzman, M. D. Dramićanin, A. Meijerink, *Nanomaterials* **2020**, *10*, 543.
[11] M. Suta, A. Meijerink, *Adv. Theory Simul.* **2020**, *3*, 2000176.

[12] D. S. Brites, R. Marin, M. Suta, A. N. Carneiro Neto, E. Ximendes, D. Jaque, L. D. Carlos, *Adv. Mater.* **2023**, *35*, 2302749.
[13] Z. Rao, X. Zhao, X. Gong, *Small* **2024**, *20*, 2406348.
[14] X. Zhang, Y. Xu, X. Wu, S. Yin, C. Zhong, C. Wang, L. Zhou, H. You, *Chem. Eng. J.* **2024**, *481*, 148717.
[15] L. A. Ramolise, S. N. Ogugua, H. C. Swart, D. E. Motaung, *Coord. Chem. Rev.* **2025**, *522*, 216196.
[16] Q. Ni, J. Huo, J. Liu, H. Yan, Q. Zhu, J. Li, C. Long, Q. Wang, *Inorg. Chem. Front.* **2022**, *9*, 6584.
[17] L. M. Cordova, Y. Zhou, G. M. Milligan, L. Cheng, T. Kerr, J. Ziller, R. Wu, M. Q. Arguilla, *Adv. Mater.* **2024**, *36*, 2312597.
[18] K. Chen, Z. Shao, C. Zhang, S. Jia, T. Deng, R. Zhou, Y. Zhou, E. Song, *Chem. Eng. J.* **2023**, *477*, 147165.
[19] H.-Y. Kai, D. Xiao, K.-L. Wong, C.-K. Duan, P. A. Tanner, *Adv. Opt. Mater.* **2025**, *13*, 2500239.
[20] J. Zhao, Y. Di, Y. Sheng, J. Sui, X. Yang, Y. Zhang, Y. Wang, H. Wang, X. Zhang, L. Yu, Z. Chen, Z. Gan, *Mater. Horiz.* **2025**, *12*, 2641.
[21] P. W. M. Jacobs, *J. Phys. Chem. Solids* **1991**, *52*, 35.
[22] W. J. L. Oomen, L. C. G. van Gorkom, W. M. A. Smit, G. Blasse, *J. Solid State Chem.* **1986**, *65*, 156.
[23] W. J. L. Oomen, W. M. A. Smit, G. Blasse, *J. Phys. C: Solid State Phys.* **1986**, *19*, 3263.
[24] X. Liu, J. Gao, Q. Wang, *Chem. Eng. J.* **2022**, *428*, 131117.
[25] T. P. van Swieten, J. M. Steenhoff, A. Vlasblom, R. de Berg, S. P. Mattern, F. T. Rabouw, M. Suta, A. Meijerink, *Light: Sci. Appl.* **2022**, *11*, 343.
[26] L. Marciniak, W. M. Piotrowski, M. Szymczak, M. Drozd, V. Kinzhybalo, M. Back, *Chem. Eng. J.* **2024**, *487*, 150363.
[27] S. Zhao, K. Sang, Y. Yang, J. Zhang, Y. Hu, M. Chen, X. Zhang, Q. Pang, L. Zhou, P. Chen, *Adv. Opt. Mater.* **2024**, *12*, 2302979.
[28] W. Yang, P. Dang, G. Zhang, D. Liu, Y. Wang, Y. Wei, H. Lian, G. Li, J. Lin, *Angew. Chem., Int. Ed.* **2024**, *63*, 202411136.
[29] X. Liu, Z. Fan, Y. Zheng, J. Zha, Y. Zhang, S. Zhu, Z. Zhang, X. Zhang, F. Huang, T. Liang, C. Li, Q. Wang, C. Tan, *ACS Appl. Mater. Interfaces* **2023**, *15*, 55991.
[30] Q. Guo, X. Zhao, B. Song, J. Luo, J. Tang, *Adv. Mater.* **2022**, *34*, 2201008.
[31] E. W. J. L. Oomen, W. M. A. Smit, G. Blasse, *Chem. Phys. Lett.* **1987**, *138*, 584.
[32] D. P. Panda, D. Swain, R. Raghunathan, A. Sundaresan, *Chem. Mater.* **2024**, *36*, 5698.
[33] Y. Zheng, X. Han, P. Cheng, X. Jia, J. Xu, X.-H. Bu, *J. Am. Chem. Soc.* **2022**, *144*, 16471.
[34] E. Herdtweck, U. Kreusel, *Acta Crystallogr. C* **1993**, *49*, 318.
[35] J. S Reuter, G. Frenzen, *Acta Crystallogr. C* **1996**, *52*, 1859.
[36] K. M. McCall, V. Morad, B. M. Benin, M. V. Kovalenko, *ACS Mater. Lett.* **2020**, *2*, 1218.
[37] Y. Toyozawa, M. Inoue, *J. Phys. Soc. Jpn.* **1966**, *21*, 1663.
[38] M. D. Ranfagni, M. B., G. V., M. P. Fontana, *Adv. Phys.* **1983**, *32*, 823.
[39] M. Bacci, A. Ranfagni, M. P. Fontana, G. Viliani, *Phys. Rev. B* **1975**, *11*, 3052.
[40] X. Wang, T. Bai, J. Sun, J. Liu, Y. Su, J. Chen, *Nano Lett.* **2024**, *24*, 14686.
[41] T. Huang, H. Peng, R. Zeng, B. Zou, *Adv. Funct. Mater.* **2025**, https://doi.org/10.1002/adfm.202511803.
[42] X. Liu, K. Li, W. Shao, W. Shen, M. Li, L. Zhou, R. He, *Inorg. Chem.* **2024**, *63*, 5158.
[43] T. Bai, X. Wang, Y. He, H. Wei, Y. Su, J. Chen, *Adv. Opt. Mater.* **2023**, *11*, 2301110.
[44] E. W. J. L. Oomen, W. M. A. Smit, G. Blasse, *Chem. Phys. Lett.* **1984**, *112*, 547.
[45] Z. Li, Y. Li, P. Liang, T. Zhou, L. Wang, R.-J. Xie, *Chem. Mater.* **2019**, *31*, 9363.
[46] E. W. J. L. Oomen, G. J. Dirksen, *Mater. Res. Bull.* **1985**, *20*, 453.
[47] E. W. J. L. Oomen, G. J. Dirksen, W. M. A. Smit, G. Blasse, *J. Phys. C: Solid State Phys.* **1987**, *20*, 1161.
[48] J. G X. Li, S. Rao, Y. Zheng, *Synth. Met.* **2017**, *231*, 107.
[49] N. Wu, A. Yu, L. Zhang, W. Liu, J. Gao, C. Zhang, Y. Zheng, *Adv. Mater. Interfaces* **2019**, *6*, 1900732.
[50] Y. He, X. Cai, X. Wang, M. B. Liisberg, J. Dostál, M. Zhang, M. Kloz, F. Gao, T. Pullerits, J. Chen, *Adv. Opt. Mater.* **2025**, *13*, 2402061.
[51] L. Zhou, J.-F. Liao, Z.-G. Huang, J.-H. Wei, X.-D. Wang, H.-Y. Chen, D.-B. Kuang, *Angew. Chem., Int. Ed.* **2019**, *58*, 15435.